

Article

Methane Dry Reforming Catalysts Based on Pr-Doped Ceria–Zirconia Synthesized in Supercritical Propanol

Marina Arapova ¹, Ekaterina Smal ¹, Yuliya Bepalko ¹, Konstantin Valeev ¹, Valeria Fedorova ¹, Amir Hassan ^{1,2}, Olga Bulavchenko ¹, Vladislav Sadykov ^{1,*} and Mikhail Simonov ¹

¹ Department of Heterogeneous Catalysis, Federal Research Center, Boreskov Institute of Catalysis, Lavrentiev Ave. 5, 630090 Novosibirsk, Russia; nemeraldo@gmail.com (M.A.); alageizia@mail.ru (E.S.); bepalko@catalysis.ru (Y.B.); valeev@catalysis.ru (K.V.); valeria@catalysis.ru (V.F.); a.khassan1@g.nsu.ru (A.H.); o.bulavchenko@catalysis.ru (O.B.); smike@catalysis.ru (M.S.)

² Novosibirsk State University, 630090 Novosibirsk, Russia

* Correspondence: sadykov@catalysis.ru

Abstract: This paper is devoted to the study of active and stable nickel catalysts for methane dry reforming based on Pr-doped ceria–zirconia obtained via the solvothermal continuous method. Studies on the physicochemical and catalytic properties of the 5%Ni/Ce_{0.75}Zr_{0.25–x}Pr_xO₂ series have showed that Pr introduction leads to an increase in the amount of highly reactive oxygen in the oxide lattice. Praseodymium-based catalysts showed significantly higher reactant conversions. In addition to the nature of support, the method of nickel introduction was also studied; Ni was added both using impregnation and the one-pot procedure with mixed oxide preparation. The method of Ni addition was shown to have significant effect on the morphology of its particles and Ni-support interaction, and, respectively, on catalytic activity and coking stability. The 5%Ni/Ce_{0.75}Zr_{0.15}Pr_{0.1}O₂ catalyst prepared by one-pot method showed stable operation in the MDR reaction for 30 h at CO₂ and CH₄ conversions of ~40% and an H₂ yield of ~18% (T = 700 °C, τ = 10 ms).

Keywords: dry reforming; methane; ceria–zirconia; supercritical synthesis; oxygen vacancies; stability



Citation: Arapova, M.; Smal, E.; Bepalko, Y.; Valeev, K.; Fedorova, V.; Hassan, A.; Bulavchenko, O.; Sadykov, V.; Simonov, M. Methane Dry Reforming Catalysts Based on Pr-Doped Ceria–Zirconia Synthesized in Supercritical Propanol. *Energies* **2023**, *16*, 4729. <https://doi.org/10.3390/en16124729>

Academic Editor: Eugenio Meloni

Received: 6 May 2023

Revised: 13 June 2023

Accepted: 14 June 2023

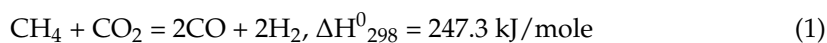
Published: 15 June 2023



Copyright: © 2023 by the authors. Licensee MDPI, Basel, Switzerland. This article is an open access article distributed under the terms and conditions of the Creative Commons Attribution (CC BY) license (<https://creativecommons.org/licenses/by/4.0/>).

1. Introduction

Methane dry reforming (MDR) is a promising way of utilizing two greenhouse gases—CH₄ and CO₂—and converting them into synthesis gas before being used as a feedstock for the chemical industry or as a fuel [1–3].



This reaction can also be effectively integrated into existing hydrogen production chains, taking into account current environmental requirements [4]. MDR catalysts are representatives of typical catalysts for hydrocarbons subject to reforming processes, which consist of a transition metal, primarily nickel, deposited on an oxide support [5]. Studies over the past few decades show that poor stability due to the sintering and carbonization of active species remains a major problem for reforming catalysts [6]. Developing a thermally stable catalyst with superior activity and enhanced resistance to carbon formation and metal sintering is among the major challenges faced by industries and researchers [7–9].

The carbonization problem begins at the stage of competition between simultaneously occurring transformation routes of CH_x intermediates on metal particles. If CH_x oxidation occurs rapidly, the formation of desired CO is observed. However, if the rate of CH_x formation is higher than its oxidation, carbon deposits grow. A well-known and highly efficient approach to increase the rate of the desired route is to involve the lattice oxygen of the support into the catalytic cycle [10,11]. The transformation of fuels over catalysts with a high oxygen reactivity occurs via the redox reaction mechanism. During the reaction, the

substrate (CH_4 and CO) is oxidized by the lattice oxygen, accompanied by the formation of a vacancy and its replenishment through the activation of the oxidizer (CO_2 , H_2O , or O_2) on the oxide surface cations and fast surface oxygen transfer to the direct catalytic zone (reverse oxygen spillover) [12,13]. The activation of highly stable CO_2 molecules can also be a rate-limiting step in MDR, which also becomes an important factor in the effective catalyst design [14].

Establishing an unambiguous relationship between the characteristics of an oxide-supported catalyst and its activity in reforming reactions is still a debated issue. In steady-state reaction conditions, its properties differ from those defined by the preparation procedure [15]. Nevertheless, a huge number of works have been carried out and described in the literature based on a complex of catalytic structural studies and DFT calculations, which showed catalytic activity correlations with the so-called «support oxygen activity» [7,16,17].

The term “support oxygen activity” is complex, including several correlated characteristics of the oxide’s lattice oxygen, such as oxygen storage capacity (OSC), surface and bulk mobility, as well as the number and formation energy of oxygen vacancies. The redox properties of oxide catalysts can be related to the content of oxygen vacancies. However, the mere presence of vacancies is not sufficient; if the vacancy formation barrier is too high, this stage becomes rate-limiting, which casts doubt on the probability of the entire process proceeding along such a route. That phenomenon, for example, was shown and confirmed by DFT calculations for nickel-containing undoped cerium oxide [18]. In the steady-state conditions of the catalytic reaction, the concentration of oxygen vacancies is determined by the ratio of the rates of both oxygen removal with the reducing agent (CH_4 , etc.) and reoxidation with the oxidant (CO_2 , etc.) [15,19]. A decrease in the energy of vacancy formation can be achieved, for example, by increasing the length of at least one oxygen bond in the lattice or by creating so-called asymmetric vacancies [20,21].

Oxides that are capable of providing cycles of lattice vacancy formation with charge compensation due to cations with a variable valence are mainly transition metal oxides, which are seen as reducible or as oxides with active oxygen [22]. Among the oxides with lattice oxygen sites that take part in the reaction, the most common are perovskites, spinels, and fluorites. Groups of oxides based on ceria doped with a wide range of cations have been extensively studied [16,23–26]. Detailed kinetic and computational studies have shown that the activity of oxygen in such oxides depends on the concentration and formation energy of these vacancies [27,28]. Moreover, it was also shown that the presence and energy of vacancies on the surface of cerium oxide can determine the oxidation of the surface intermediate $-\text{CO}$ into CO_2 , thus largely determining the H_2/CO ratio in the resulting synthesis gas [29,30]. One of the most popular doping cations which also increases the thermal stability of CeO_2 oxide is Zr [31,32]. The praseodymium cation has a size similar to that of the cerium cation and is capable of replacing the latter in the oxide crystal lattice. In this case, micro-distortions are formed and the number of anion vacancies can potentially increase, which can favorably affect the catalytic activity. The effective generation of asymmetric vacancies in CeO_2 -based oxides upon being doped with Pr, increasing the oxygen catalytic activity, has been shown in a number of studies [18,33–35]. Furthermore, the substitution of no more than 25% of cerium has been shown to be effective since the Pr extent would result in the clustering of oxygen vacancies [20,22].

The synthesis of these polycation oxides for catalytic application should provide a high chemical uniformity and oxide dispersion. Coprecipitation [36], hydrothermal method [37], solvothermal method [38], sol–gel–citrate [39,40] and ester polymer precursors (Pechini) [41], microemulsions [42], the microwave method [43,44], the sonochemical method [45], solution combustion [46,47], and spray pyrolysis reactions [48] are all known methods. The use of the solvothermal method for the synthesis of such polycationic oxides provides structural homogeneity, as well as improved textural characteristics and tunable particle size distributions [49]. Moreover, synthesis with the use of supercritical fluids is characterized by a lower energy consumption and simple implementation. The mechanism of oxide formation during hydrothermal synthesis includes two stages: the hydrolysis of

metal ions and their precipitation in the form of oxides as a result of dehydration at high temperatures [50,51]. Supercritical alcohols are of interest as solvents because they have lower critical temperatures and pressures than water, and the conditions for reaching the supercritical state that vary depending on the nature of the alcohol. The use of supercritical alcohols contributes to a high rate of nucleation with the slight subsequent growth of the formed nuclei, which makes it possible to obtain highly dispersed oxide particles [52]. Thus, varying the temperature and pressure makes it possible to influence the nucleation rate and synthesize samples with desired characteristics. In our previous study [53], it was shown that synthesis in supercritical isopropanol makes it possible to obtain single-phase mixed Ce-Zr-(Ti/Nb) oxides, in contrast to the Pechini method.

It is important to emphasize the decisive influence of the nickel introduction method. In an oxide–metal system, the dispersion of supported metallic particles and the strength of its interaction with additional support are key properties that determine catalyst stability in reforming reactions on a par with the support oxygen activity [54–56]. It was shown that the traditional method of wet impregnation is less efficient than the method of nickel that is introduced into the oxide structure at the stage of support synthesis. In the second case, during the reduction pretreatment, finely dispersed metal particles strongly bound with support are formed [57,58]. At the same time, a part of the active component can remain in the bulk of support that is not accessible for reagents.

Hence, the use of zirconium as a doping cation to ceria increases the stability of the structure and increases the structure defectiveness, while doping with praseodymium increases the concentration of oxygen vacancies and the reactivity of the surface oxygen. Accordingly, in this study, our goal was to synthesize a series of complex metal–oxide catalysts $5\%Ni/Ce_{0.75}Zr_{0.25-x}Pr_xO_2$ obtained using the solvothermal method with Ni added by both impregnation and the one-pot method. This study presents results on the study of $5\%Ni/Ce_{0.75}Zr_{0.25-x}Pr_xO_2$ textural and redox properties and their effect on catalytic activity and stability in the MDR reaction.

2. Materials and Methods

2.1. Synthesis Methods

The catalyst supports were synthesized in supercritical alcohol media using original installation described in more detail earlier [53,58]. Cerium nitrate $Ce(NO_3)_3 \cdot 6H_2O$ (Vekton, Petersburg, Russia), praseodymium nitrate $Pr(NO_3)_3 \cdot 6H_2O$ (Vekton, Russia), and zirconium butoxide (80 wt% in n-butanol, Alfa Aesar, Karlsruhe, Germany) were dissolved in required proportions in isopropanol (Reakhim, St. Petersburg, Russia). Then, the solution was fed into the reactor and synthesis was carried out according to the method described earlier [53]. For impregnated catalysts, nickel was supported by the incipient wetness impregnation of supports with the water solution of $Ni(NO_3)_2$ (Vekton, Russia) [54].

For one-pot catalysts, nickel nitrate $Ni(NO_3)_2 \cdot 6H_2O$ (Vekton, Russia) was dissolved together with Ce and Zr (Pr) salts, and synthesis in a supercritical medium was carried out, according to the procedure described above. All catalysts were dried at 200 °C and calcined at 700 °C for 2 h. The loading amount of Ni was 5 wt% both for the impregnated and one-pot catalysts. The prepared sample denotations are presented in Table 1.

2.2. Characterizations

The specific surface area (SSA) was defined by the BET method using a Quadrasorb evo (Quantachrome Instruments, Boynton Beach, FL, USA) installation. The pore volumes and pore size distributions were determined from the desorption branch of the isotherm using the BJH method.

XRD analysis was performed on a Thermo X'tra diffractometer, in the angle range of 20–85° with a step of $2\theta = 0.02^\circ$ and a speed of $1^\circ/\text{min}$, using a Mythen2R 1D linear detector (Decstris, Switzerland). The $CuK\alpha$ radiation ($\lambda = 1.5418\text{\AA}$) was used. The average sizes of coherent scattering regions (CSRs) were calculated using the Scherrer formula from

the 111 fluorite reflection. A description of the diffraction profile was made using the Fityk program with the Lorentz function.

Table 1. The sample's designation, specific surface area (SSA), pore volume (V_{pore}), and Fm3m lattice parameter (a).

Designation	Ni Addition Method	Composition	SSA, m ² /g	V_{pore} , cm ³ /g	a *, Å
CZP	-	Ce _{0.75} Zr _{0.15} Pr _{0.1} O ₂	14	0.055	5.403(1)
N/CZP	Impregnation	5%Ni/Ce _{0.75} Zr _{0.15} Pr _{0.1} O ₂	9	0.095	5.397(1)
N+CZP	One-pot	5%Ni+Ce _{0.75} Zr _{0.15} Pr _{0.1} O ₂	14	0.081	5.407(1)
CZ	-	Ce _{0.75} Zr _{0.25} O ₂	29	0.150	5.369(1)
N/CZ	Impregnation	5%Ni/Ce _{0.75} Zr _{0.25} O ₂	21	0.144	5.373(1)
N+CZ	One-pot	5%Ni+Ce _{0.75} Zr _{0.25} O ₂	13	0.126	5.372(1)

*—lattice parameter of the fluorite phase estimated from XRD data.

XRD with H₂ in situ analysis was conducted using a Bruker D8 Advance diffractometer (Germany), in the angle range of 20–55° with a step of $2\theta = 0.05^\circ$ and an accumulation time of 3 s at each point using a LynxEye (1D) line detector. The monochromatic CuK α radiation ($\lambda = 1.5418\text{Å}$) was used. The measurements were carried out using an XRK-900 high-temperature reactor chamber (Anton Paar, Graz, Austria). The 10%H₂/90%He mixture at a flow rate of 100 mL/min was passed through the chamber during heating and cooling to room temperature. Heating was carried out based on the following scheme: 250, 315, 400, 500, 700, and 30 °C, with a heating rate of 12°/min. The lattice parameters and phase relationships were refined with the Rietveld method [59]. In the refinement, the CeO₂ structure was used; only the Ce atoms were in the cationic position.

The Raman spectrometer T64000 (Horiba Jobin Yvon, Kyoto City, Japan) with micro-Raman setup was used to record the Raman spectra. All experimental spectra were collected in the backscattering geometry using the 514.5 nm line of an Ar⁺ laser. The spectral resolution was not worse than 1.5 cm⁻¹. The detector was a silicon-based CCD matrix, cooled with liquid nitrogen. The power of the laser beam reaching the sample was 2 mW. The band at 520.5 cm⁻¹ of the Si single crystal was used to calibrate the spectrometer.

TEM with EDX. Transmission electron microscopy (TEM) micrographs were obtained with a Themis-Z 3.1 instrument (TFS, Durham, NC, USA), equipped with a X-FEG-monochromator and a CS/S double corrector (with an accelerating voltage 200 kV), as well as a JEM-2200FS transmission electron microscope (JEOL Ltd., Akishima City, Japan, Japan, acceleration voltage 200 kV, lattice resolution ~1 Å), equipped with a Cs corrector. Elemental analysis was performed with a Super-X EDS detector (with an energy resolution of about 120 eV) in HAADFSTEM mode. Samples for the TEM study were prepared for ultrasonic dispersion in ethanol and for the subsequent deposition of suspension in a “holey” carbon film supported on a copper grid.

TPR-H₂. Temperature-programmed reduction using hydrogen was carried out from 25 °C to 900 °C in a flow installation with a Tsvet 500 (JSC Tsvet, Kostroma, Russia) thermal conductivity detector using 10 vol. % H₂ in Ar feed at a flow rate of 40 mL/min.

The total H₂ consumption was calculated by integrating the area under the curve.

Ni reducibility was calculated with the formula:

$$\text{Reducibility} = \frac{H_2(\text{catalyst}) - H_2(\text{support}) \cdot 0.95}{0.85} \cdot 100\%$$

where H₂ (catalyst) and H₂ (support) [mmol H₂/g]—the amount of hydrogen consumed for catalyst and support reduction, respectively; 0.95—the support content in the catalyst; 0.85 [mmol H₂/g]—the theoretical amount of H₂ needed to reduce all supported Ni.

2.3. Catalytic Tests

The catalysts were preliminary reduced in a stream of 5% H₂ in He at 600 °C for 1 h. Catalytic activity in methane dry reforming reaction was studied using a tubular quartz plug flow reactor and a gas analyzer with IR sensors for CO, CO₂, and CH₄, and an electrochemical sensor for H₂ (Boner LLC, Novosibirsk, Russia). Studies were conducted with an initial mixture of 15% CH₄ + 15% CO₂ + 70% N₂ in the temperature range of 600–750 °C and a contact time of 10 ms. Long-term stability tests were carried out for 30 h at 700 °C.

The equilibrium values of reactant conversions and product yields were calculated by minimizing the Gibbs energy.

3. Results

3.1. Textural and Structural Features

Table 1 lists the designation, chemical composition, and specific surface area (SSA) of the obtained samples.

As can be seen, the samples obtained did not have a very high specific surface area; the values of SSA for the entire series of samples were about 10–30 m²/g, despite the fact that the nitrogen adsorption–desorption isotherms (Figure 1a) for all samples corresponding to the IV type were characteristic for mesoporous materials [60,61]. The introduction of praseodymium reduced the specific surface area of the initial support from 29 m²/g for CZ to 14 m²/g for CZP. This correlates well with data on the pore's size distribution for supports (Figure 1b), where the number of mesopores less than 5 nm for praseodymium-doped sample was significantly reduced. In contrast, for samples prepared by the one-pot method (N+CZ and N+CZP), there was no difference in the SSA values. The pore volume was also reduced with the introduction of praseodymium from 0.126–0.150 cm³/g for undoped samples to 0.055–0.095 cm³/g for samples with Pr. The micropore ($D \leq 2$ nm) volume was negligible for all samples and did not exceed 0.003 cm³/g.

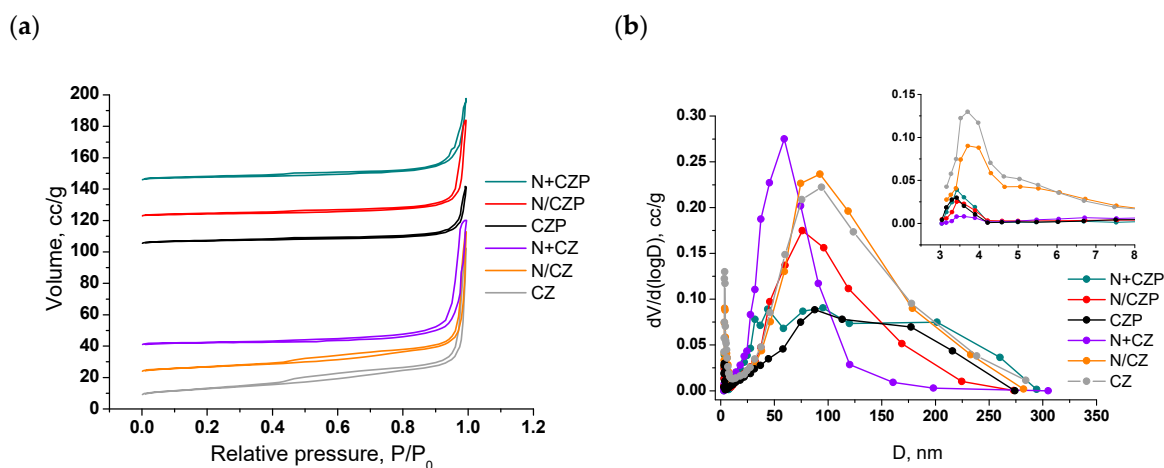


Figure 1. N₂ adsorption–desorption isotherms (a) and pore size distributions (b) for the supports and Ni-containing samples. Isotherms were separated by height for the convenience of readers.

According to XRD data (Figure 2), for the entire series, the main intense peaks located at $2\theta = 28.7, 47.7, 56.6, 59.4, 69.8, 77.0,$ and 79.4° corresponded to 111, 200, 220, 311, 222, 331, 420, and 422 reflections of the fluorite structure Fm3m (PDF 81–0792). There were no reflections of Zr and Pr individual oxides for the entire series. For the Pr-containing samples, the absence of double peaks and the shift in the fluorite peaks to the lower angles' region (Figure 2, Table 1) suggest that praseodymium was embedded in the CZ cubic structure, which is consistent with data in the literature [25,62]. The ability of praseodymium to replace cerium without destroying the fluorite structure was ensured by the close radii of cations of the same valencies ($\text{Ce}^{4+} = 1.110 \text{ \AA}; \text{Pr}^{4+} = 1.100 \text{ \AA}; \text{Ce}^{3+} = 1.283 \text{ \AA}; \text{Pr}^{3+} = 1.266$

Å), and a slightly higher $\text{Pr}^{4+}/\text{Pr}^{3+}$ redox potential led to the formation of a structure with more active oxygen compared to undoped ones [62,63]. For N/CZ, N/CZP, and N+CZP, small peaks located at $2\theta = 37.47, 43.36,$ and 62.83° corresponding to 111, 200, and 220 reflections of NiO (PDF 471049) were detected. It is worth mentioning that for N+CZ, a slight increase in the background was observed in the positions of 111 and 200 reflections of NiO, indicating the presence of highly dispersed particles of nickel oxide. The crystallite size of NiO (the average size of a coherent scattering region (CSR)) was estimated using the Scherrer equation for 200 peak analysis. The CSR values of NiO for N/CZP, N/CZ, and N+CZP were 23, 27, and 10 nm, respectively. Hence, one-pot synthesis provided smaller crystallites of NiO than the impregnation route.

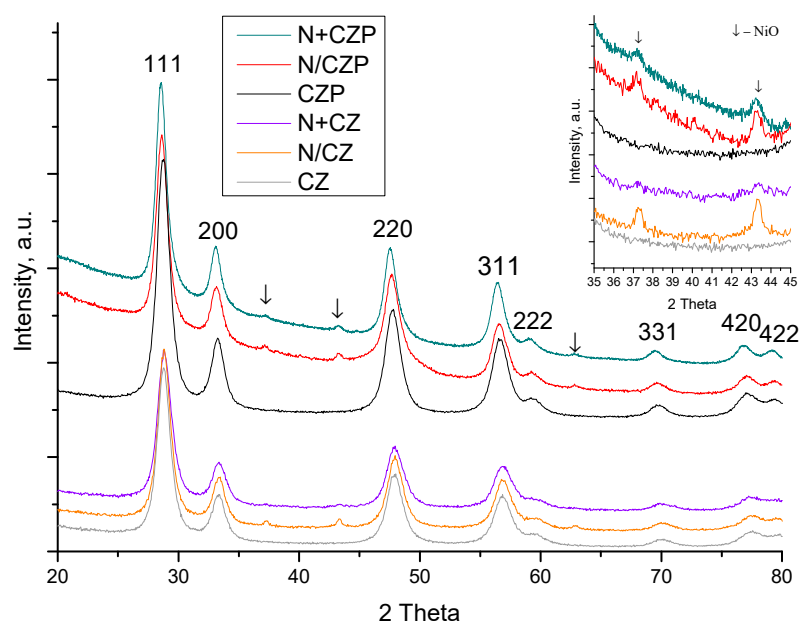


Figure 2. Diffraction pattern of supports and Ni-containing samples. Reflections of the fluorite structure are marked by (hkl) indices; the arrows indicate the NiO reflections.

Raman spectroscopy was used to investigate vibrations in the oxygen lattice and crystalline symmetry in addition to XRD analysis, since this method is more sensitive to the microstructure of materials. Figure 3 presents the Raman spectra of the investigated samples. The main fluorite structure band in pure ceria was located at 464 cm^{-1} and corresponded to the F_{2g} active mode that appears due to the symmetric stretching vibration of O anions around each Ce^{4+} cation [40]. This band was very sensitive to any changes in oxygen sublattice; therefore, with a change in the chemical composition or defect's concentration, the band shifted to lower or higher energies. For our samples, the incorporation of smaller Zr^{4+} cation led to the F_{2g} band being shifted to higher wave numbers, while the incorporation of close-size praseodymium shifted it to lower wave numbers, which is in good agreement with data in the literature and also confirms the incorporation of doped cations in the fluorite lattice [40,62]. Such a strong shift in the case of Pr cation was probably connected with the increased structure distortion [62].

For catalysts obtained by Ni impregnation (N/CZ and N/CZP), the F_{2g} band practically retained its position. However, Ni addition at the stage of mixed oxide preparation (N+CZ and N+CZP samples) resulted in the incorporation of Ni cations in the fluorite structure and further shifts in this band. In addition to the F_{2g} mode, there was a band around 570 cm^{-1} (D band) corresponding to the non-degenerate longitudinal optical (LO) mode due to the presence of defects in the fluorite lattice, resulting from the formation of oxygen vacancies [62,64]. The ratio of D and F_{2g} band areas $\omega = \text{D}/\text{F}_{2g}$ can be considered

as a parameter that is sensitive to structure defectiveness and the amount of oxygen vacancies [40,58,62]. Its values for investigated samples are presented in Figure 3 in black frames.

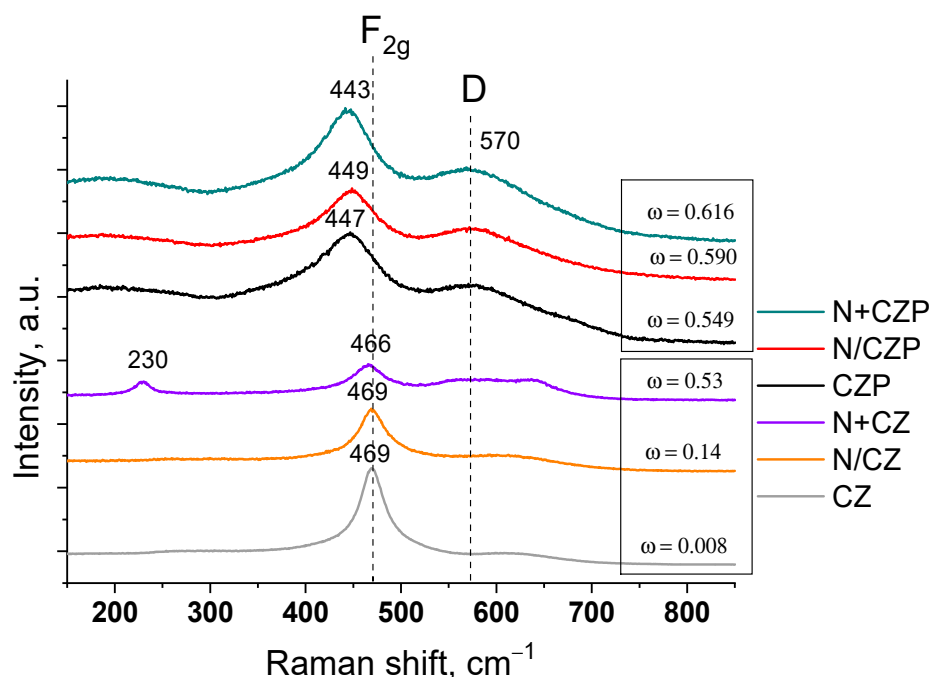


Figure 3. Raman spectra of supports and Ni-containing samples.

It can be seen that ω values increased significantly with the introduction of praseodymium (more than 50 times for supports and 4 times for impregnated catalysts). This confirms that Pr incorporation leads to increased amounts of oxygen vacancies in the fluorite structure. The introduction of nickel with any of the methods used led to an increase in the number of vacancies due to its partial incorporation into the fluorite lattice, and this effect was especially noticeable for both one-pot catalysts, for which ω values were close. The low-intensity band at 230 cm^{-1} for one-pot N+CZ could be assigned to the transverse acoustic (TA) mode, which was also connected with defects in the fluorite structure [40,64].

The method of adding nickel had a strong effect on the oxide's morphology. XRD (Figure 2) and TEM data (Figure 4) show that the deposition of nickel via wet impregnation on the formed oxide resulted in the formation of large well-crystallized NiO particles (about 20 nm in size, weakly bound to the support). For these samples, there were peaks at $2\theta = 37.4, 43.3,$ and 62.8° , which could be associated with the 111, 200, and 220 reflections of nickel oxide NiO (Fm3m). The introduction of nickel in the supercritical conditions led to the incorporation of a significant amount of nickel into the fluorite structure and the formation of residual finely dispersed NiO particles firmly fixed on the oxide surface or encapsulated into it.

The images of HAADF-STEM with EDX analysis show the distribution of elements in the particles of the one-pot N+CZP catalyst (Figure 5). As in our previous works [58], the synthesis of one-pot catalysts under supercritical conditions allowed us to obtain a homogeneous distribution of cations. Ce, Zr, and Pr cations of the support, as well as Ni cations, were uniformly distributed in the structure of $\text{Ni}+\text{Ce}_{0.75}\text{Zr}_{0.15}\text{Pr}_{0.1}\text{O}_2$.

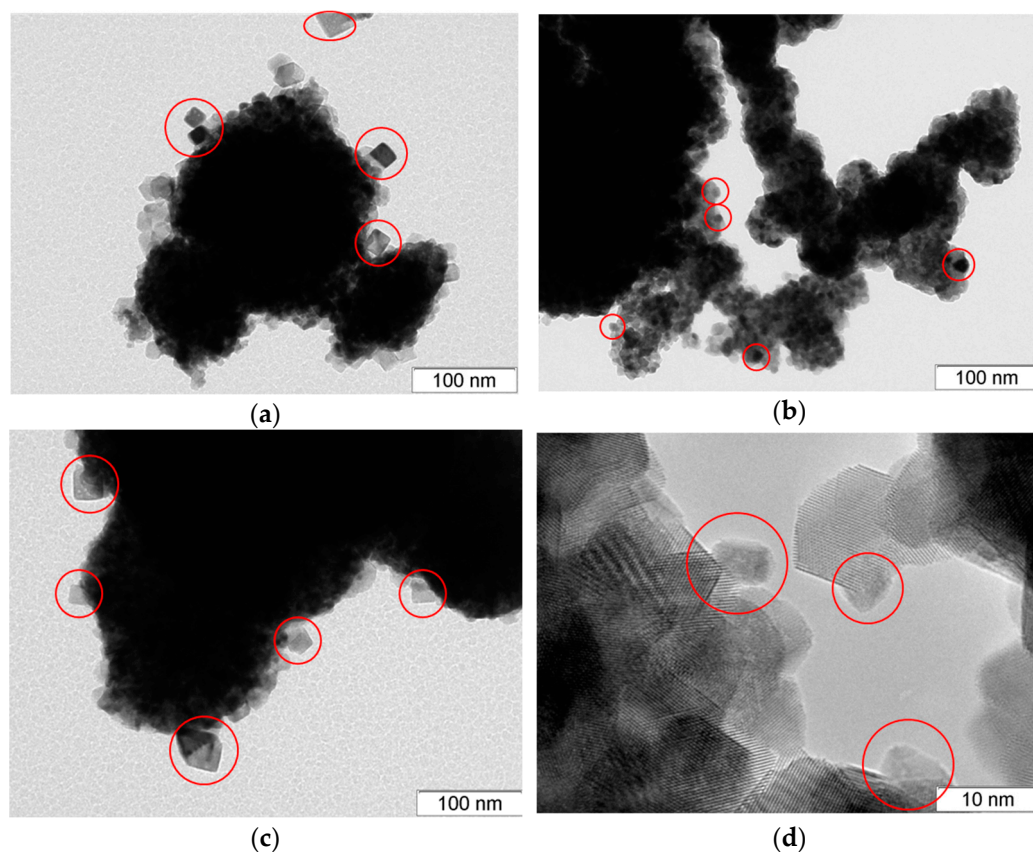


Figure 4. TEM: (a,c) impregnated Ni/CZP; (b,d) one-pot N+CZP. NiO nanoparticles are marked by red circles.

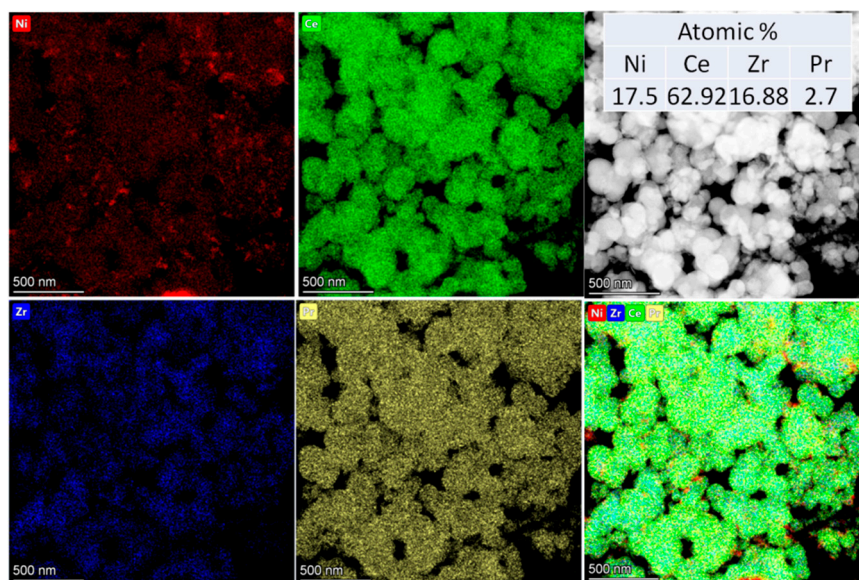


Figure 5. HAADF-STEM image with the EDX analysis of one-pot N+CZP.

3.2. Reducibility and Oxygen Reactivity

The oxide's oxygen activity was estimated by a combination of complementary methods—TPR-H₂ and XRD—with in situ H₂ reduction. The TPR-H₂ results are presented in Figure 6 and Table 2.

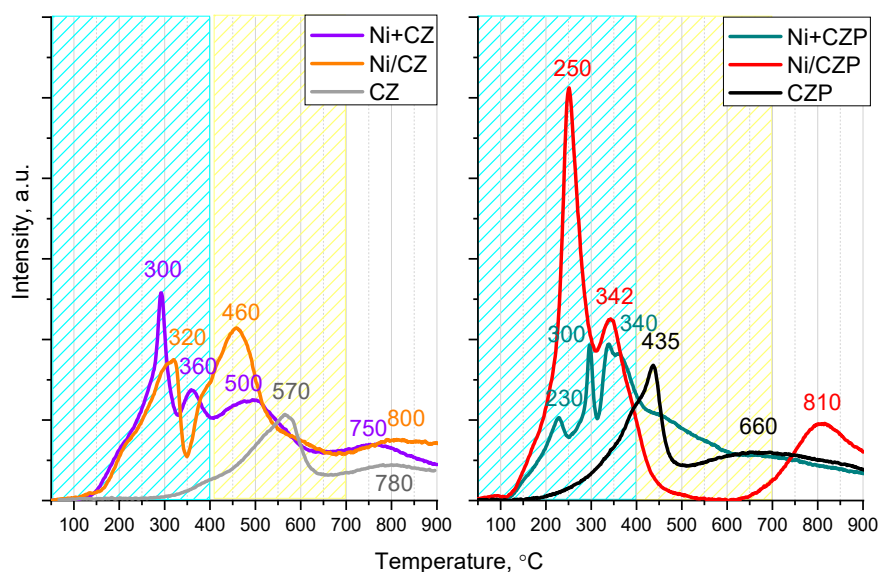


Figure 6. TPR-H₂ patterns for the supports and Ni-containing samples.

Table 2. Hydrogen consumption calculated from TPR-H₂ results.

Sample	H ₂ Consumption, mmol H ₂ /g _{cat}	Ni Reducibility, %
CZP	1.21	-
N/CZP	2.14	117
N+CZP	1.84	81
CZ	1.36	-
N/CZ	2.21	108
N+CZ	2.03	87

The curves of two supports (CZ and CZP) represent two standard reduction regions for these oxides: the medium-temperature region at 300–600 °C, related to the reduction of more reactive surface oxygen, and the high-temperature region above 700 °C, corresponding to the reduction of bulk oxygen, limited by internal diffusion. It can be seen that for the Pr-doped support, both the start of reduction and the maximum of the first peak shifted by about 200 °C towards lower temperatures, which indicates the significant facilitation of the reduction of surface oxygen with doping.

However, significant changes in the nature of reduction were noted with the introduction of praseodymium and nickel to CZ. For the N/CZP- and N/CZ-supported samples, the most intense sharp peak was located at 250 °C for the Pr-doped one and was shifted by 70 °C relative to the undoped sample, reaching its maximum at 320 °C. In situ XRD data (Figure 7b,c) show that at this temperature, there was an intense change in the fluorite parameter and no formation of metallic nickel particles was observed. This allowed us to attribute this peak to the reduction of the active oxygen of the oxide, located at 435 and 570 °C for the CZP and CZ supports, respectively. A shift in this peak to lower temperatures for Ni-containing samples was observed in most studies and was associated with the facilitation of oxide reduction due to hydrogen spillover in the presence of nickel atoms. Calculating the total amount of hydrogen consumed over the entire temperature range shows that the Ni reducibility (Table 2) for this samples exceeded 100% because the formation of metallic nickel particles led to an increase in the depth of carrier reduction due to hydrogen spillover [65].

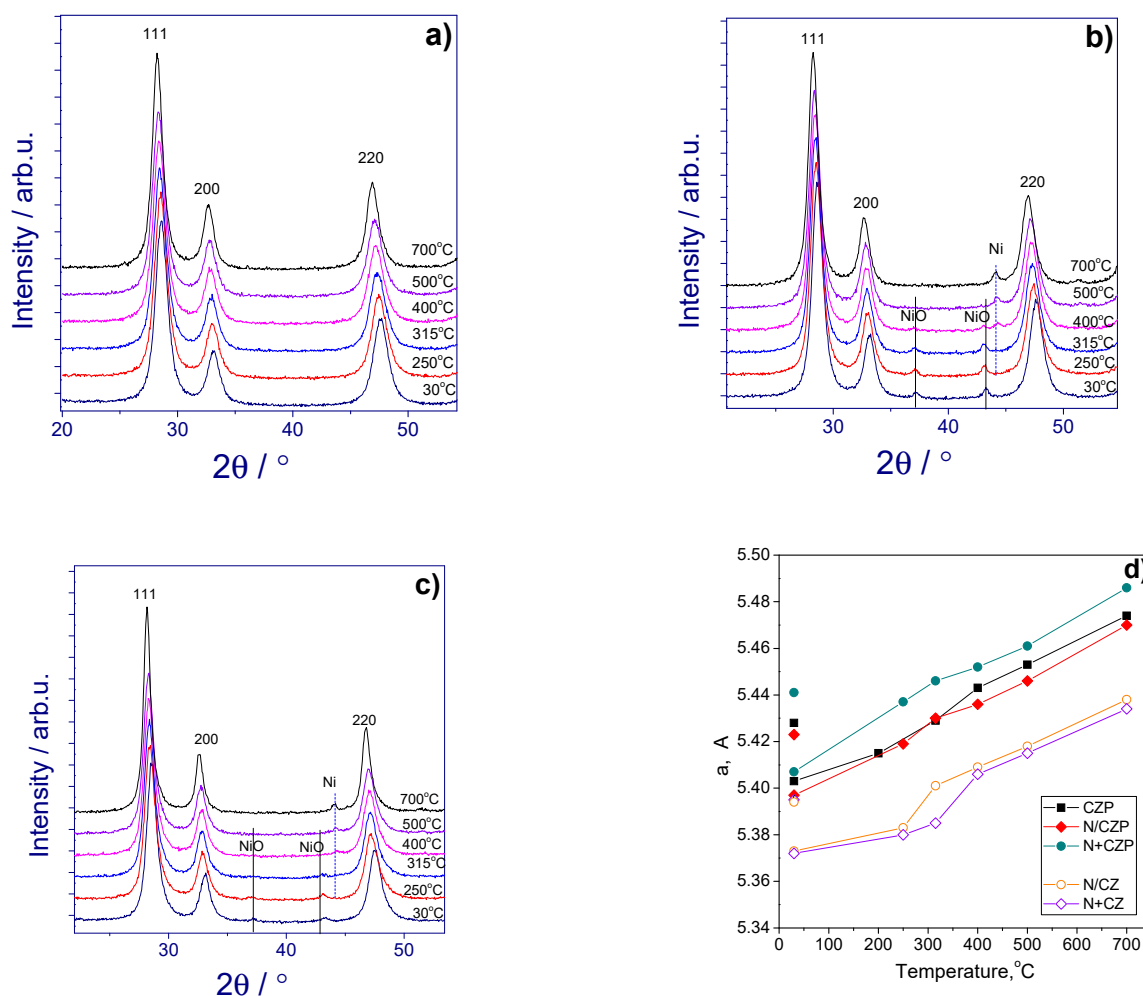


Figure 7. Diffraction patterns recorded during in situ reduction: (a) CZP; (b) N/CZP; (c) N+CZP. The reflections of the fluorite structure are labeled; the positions of NiO peaks are indicated by solid lines and those of Ni are indicated by dotted lines. (d) Fluorite lattice parameters versus temperature.

For the one-pot N+CZP and N+CZ samples, reduction occurred more uniformly in the range of 200–400 °C and the curves had a complex contour because of the simultaneous reduction of fluorite and nickel from the oxide, which is more strongly associated with the support. Lower Ni reducibility for one-pot samples also indicated a strong interaction of nickel with the support and its partial dissolution in the volume of fluorite.

XRD with in situ H_2 reduction (Figure 7a–c) confirmed that, after reduction at 400 °C, a significant amount of metallic nickel ($2\theta = 44.2^\circ$) was detected for all nickel-containing samples. Moreover, in the temperature range of 400–500 °C, the intensity of nickel reflections for supported catalysts was higher compared to that of one-pot samples, which is consistent with the TPR- H_2 data and the assumption that nickel is partially incorporated into the fluorite lattice in one-pot samples. According to XRD with in situ H_2 reduction data (Figure 7a), the phase composition of the CZP sample did not change under reductive conditions. However, the lattice parameter of oxide increased from 5.403(1) to 5.474(1) Å during heating from RT to 700 °C, while the parameter did not return to the initial value after cooling and was equal to 5.428(1) Å (Figure 7d). An increased value of the lattice parameter can probably be explained by the partial reduction of cations. In the case of N/CZP and N+CZP, a similar effect was observed. The differences in the lattice parameters between the initial state and after reduction were 0.027 Å and 0.037 Å. Such an evolution of lattice parameters could be explained by the exsolution of Ni cations from the structure of a solid solution ($\text{Ce}^{4+} = 1.110 \text{ \AA}$; $\text{Pr}^{4+} = 1.100 \text{ \AA}$; $\text{Ce}^{3+} = 1.283 \text{ \AA}$; $\text{Pr}^{3+} = 1.266 \text{ \AA}$; $\text{Ni}^{2+} = 0.69 \text{ \AA}$)

and/or differences in the reducibility of catalysts prepared by the one-pot method and impregnation. Interestingly, the behavior of lattice parameters differed for CZ and CZP catalysts, indicating the role of Pr addition. For N/CZ and N+CZP, the evolution of fluorite cell parameters almost coincided with temperature. In the initial state, the lattice parameter of the mixed oxide was 5.372(1) Å, and after reduction it was 5.394(1) Å, i.e., the difference between the states was 0.022 Å.

XRD with in situ H₂ (Figure 7d) reduction also showed a non-linear change in the lattice parameter in the temperature range of 200–400 °C, where hydrogen interacted with the most reactive oxide's oxygen. Stronger parameter changes in this region for Pr-containing catalysts compared to undoped ones confirmed the facilitation of the release of lattice oxygen obtained by the TPR-H₂ method with Pr doping. A noticeable overstating value of the lattice parameter at 300–400 °C coincided with the appearance of nickel metallic reflections on XRD patterns, and indicated a greater depth of reduction due to the well-known phenomenon of hydrogen spillover described in the literature [65–68]. It is also important to note that after returning to room temperature, the Fm3m fluorite monophase was preserved with an increased parameter; hence, the release of oxygen occurred without destroying the structure.

3.3. Catalytic Activity in MDR

The results of MDR catalytic experiments are shown in Figure 8. Before testing, a blank experiment was carried out with an equivalent to the catalyst's amount of quartz; no reactants were converted and no products were formed over the entire temperature range. A carbon balance calculated for all experiments was not lower than 95%. For all samples, an increase in the conversions of methane and carbon dioxide was observed with increasing temperature in accordance with the endothermicity of the reaction.

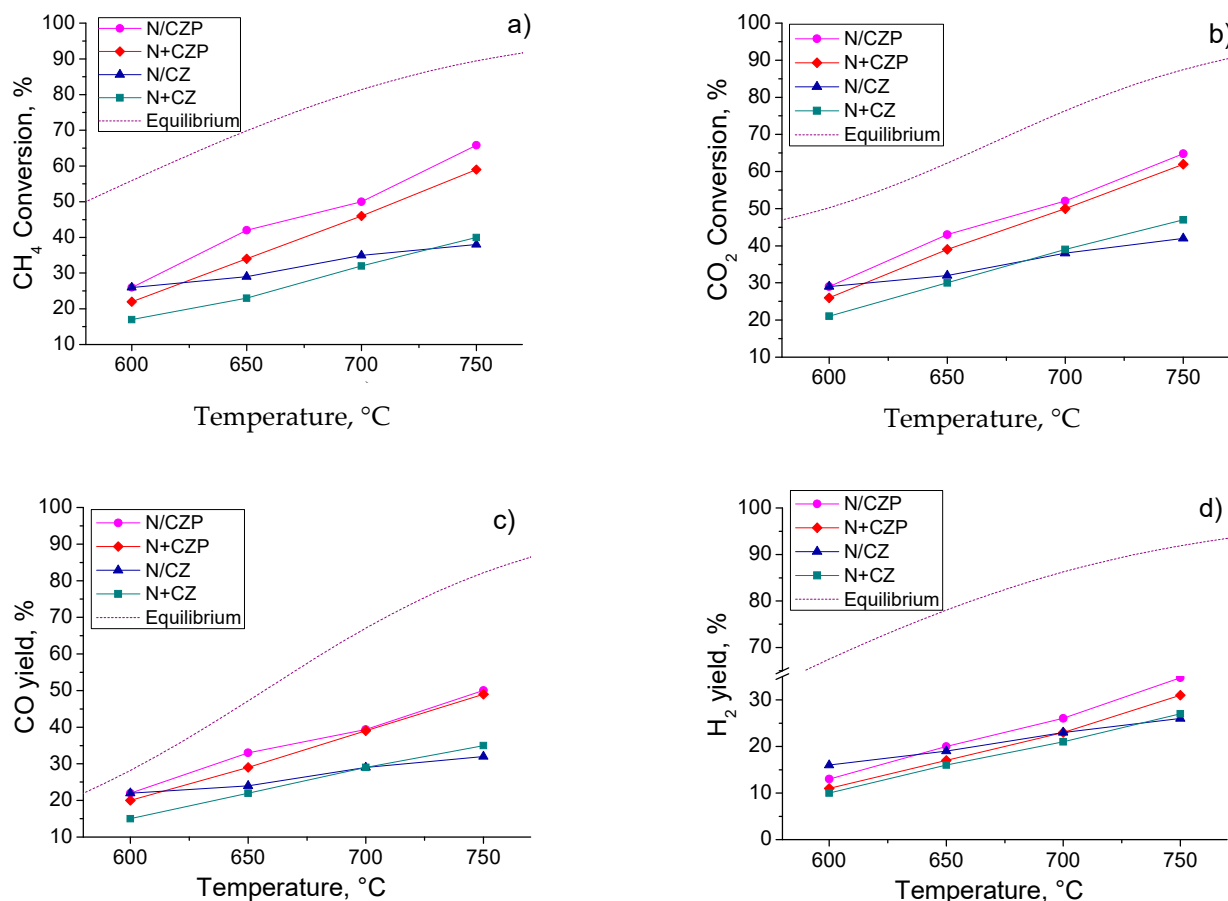


Figure 8. Cont.

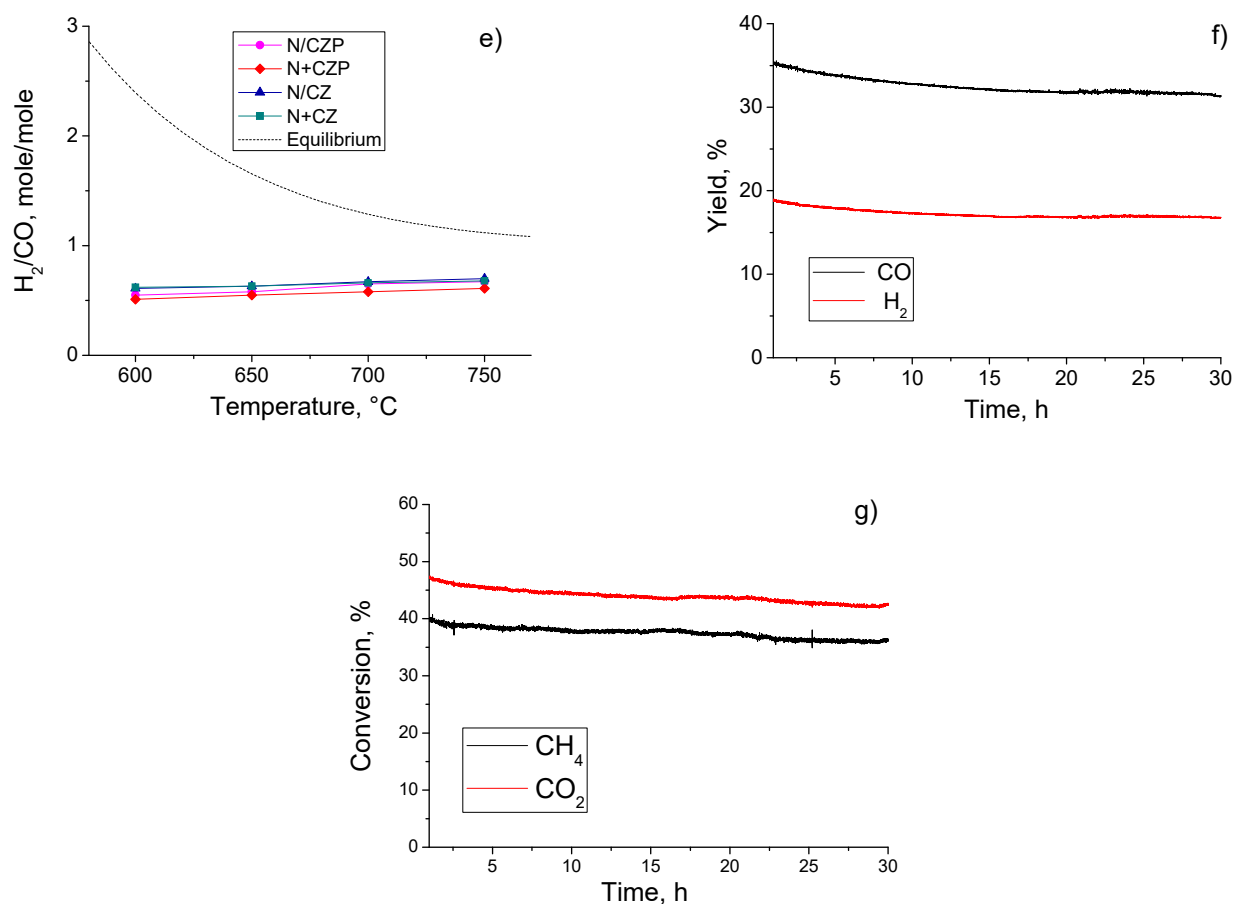


Figure 8. Catalytic test results for the N/CZ(P) and N+CZ(P) catalysts in methane dry reforming catalysts: temperature dependences of (a) CH_4 conversion (b) CO_2 conversion; (c) CO yield, (d) H_2 yield, (e) H_2/CO ; (f) H_2 and CO yields; and (g) CH_4 and CO_2 conversions in long-term tests for N+CZP one-pot catalyst at 700 °C. Catalyst grain size 0.25–0.5 mm, contact time 10 ms, $C^0(CH_4) = C^0(CO_2) = 15\%$.

The activity of Pr-containing catalysts N/CZP and N+CZP exceeded the activity of samples based on undoped CZ support, and the difference significantly increased with an increase in temperature. This is consistent with literature data describing an increase in the contribution of support to the reaction with the temperature increase due to the more efficient activation of CO_2 and the transfer of active oxygen forms over the oxide surface to the metal–support interface [29,30].

At the same time, the method of introducing nickel did not noticeably affect the activity in experiments with temperature variation, but strikingly determined stability in the long-term tests. For the N/CZP sample obtained by wet impregnation, reactor plugging occurred within 1 h of a long test at 700 °C (not shown on Figures) due to carbon formation. Figure 8f shows data on the H_2 and CO yields in long-term tests for the N+CZP one-pot catalyst. After 30 h of the reaction, the hydrogen yield decreased from 35 to 32% and the CO yield decreased from 19 to 17%, and the main drop occurred for the first 3 h of the reaction. The catalyst after 30 h of reaction was investigated by TPO and was shown to be free of carbon.

The TEM studies of catalysts after catalytic tests in the temperature range of 600–750 °C showed that the N/CZP sample was characterized by whisker carbon deposits and weak bonds between nickel and the support resulted in the detachment of nickel particles from the surface, while the N+CZP sample demonstrates that metal particles were firmly fixed on the oxide surface and that an insignificant number of thin layers of carbon were directly fixed on the metal particles, which do not block active catalytic centers (Figure 9).

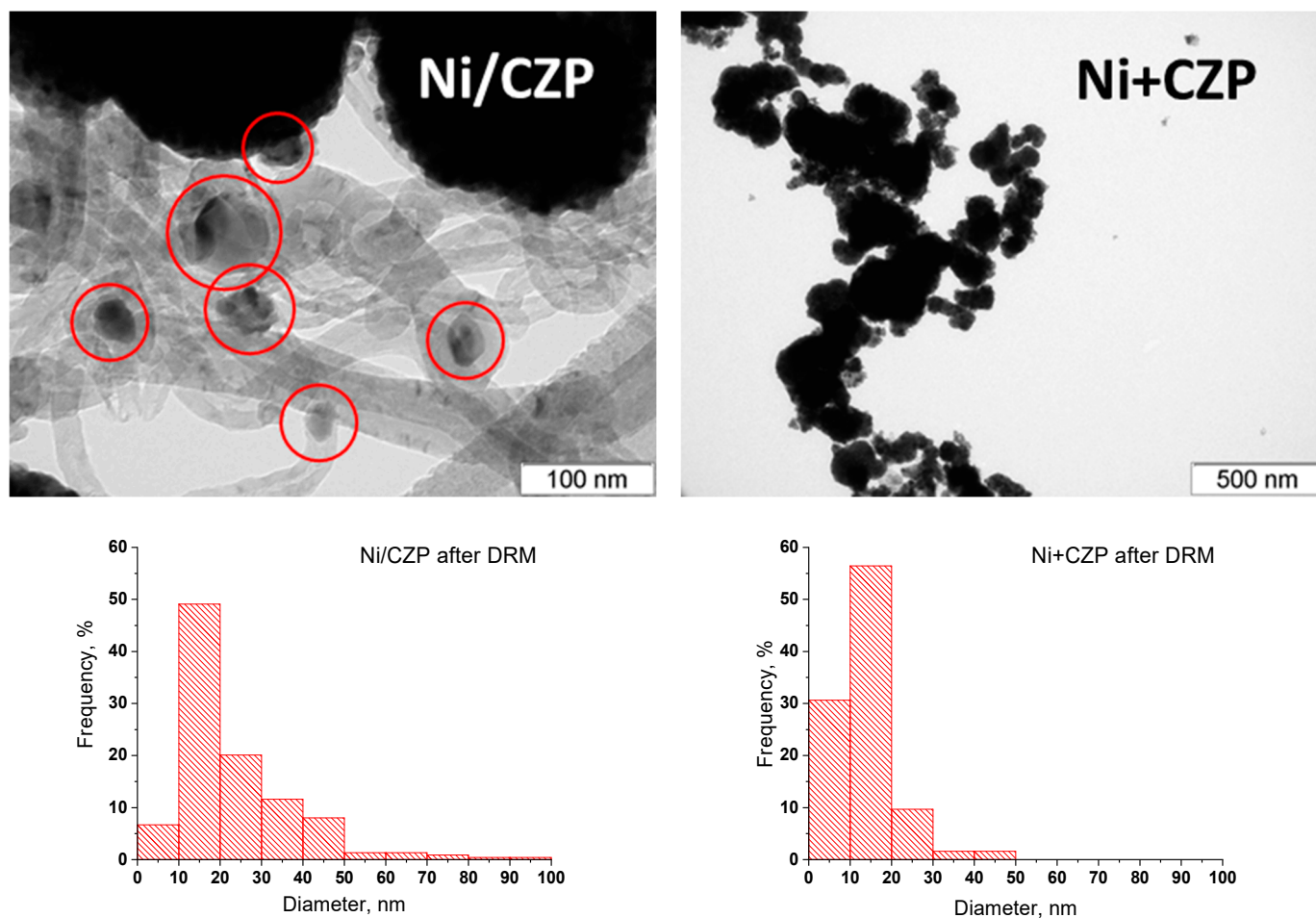


Figure 9. TEM images and particle size histograms of Ni/CZP and Ni+CZP catalysts after the reaction. Nickel particles are marked with circles.

Hence, the catalytic activity of samples modified with praseodymium was significantly higher than that of the unmodified ones. An increase in the conversion of both methane and CO_2 correlated with an increase in the activity of the carrier's highly reactive oxygen, as shown by the TPR- H_2 method. Moreover, as was shown by Raman spectroscopy, Pr-doped samples contained a higher number of defects and oxygen vacancies (i.e., sites for CO_2 activation). At the same time, stability of the catalyst was dramatically affected by the strength of the interaction of resulting nickel metal particles with the oxide support. Thus, for samples obtained by wet impregnation, the weak bond with the support, shown by TEM and TPR- H_2 methods, eliminated all the advantages of the active support and prevented the effective occurrence of the redox mechanism, leading to rapid deactivation with the formation of a significant amount of fibrous carbon deposits, as confirmed by TEM images. For samples with nickel introduced at the stage of support formation, high stability after 30 h of the reaction at 700 °C and the absence of carbon deposits were shown.

A comparison of data on the catalytic activity in the DRM reaction with literature analogues under similar conditions (Table 3) indicates the significant potential of the praseodymium-modified sample synthesized under supercritical conditions.

Table 3. A comparison of the methane conversion ($X(\text{CH}_4)$) obtained at 700 °C with literature analogues.

Catalyst	Reaction Conditions	τ , ms	$X(\text{CH}_4)$ at 700 °C, %	Ref
Ni/Ce _{0.5} Zr _{0.5} O ₂	CH ₄ = 20% CO ₂ = 20% N ₂ = 60%	120	15	[25]
Ni/Ce _{0.75} Ti _{0.05} Nb _{0.05} Zr _{0.15} O ₂	CH ₄ = 15% CO ₂ = 15% N ₂ = 70%	10	30	[53]
Ni/ZrO ₂	CH ₄ :CO ₂ :N ₂ = 3:3:1	~90	56	[69]
Ni/ZrO ₂ -Al ₂ O ₃	CH ₄ :CO ₂ = 1	~150	38	[70]
5%Ni/Y+Zr	CH ₄ :CO ₂ :N ₂ = 3:3:1	~90	67	[71]
5%Ni/La+Zr	CH ₄ :CO ₂ :N ₂ = 6:6:1	~90	66	[72]
Ni/Ce _{0.75} Pr _{0.1} Zr _{0.15} O ₂	CH ₄ = 15% CO ₂ = 15% N ₂ = 70%	10	39	This work

4. Conclusions

In this work, catalysts series 5%Ni/Ce_{0.75}Zr_{0.25-x}Pr_xO₂ ($x = 0; 0.1$) were successfully synthesized by the solvothermal method in a flow-through setup in supercritical isopropanol. All samples were found to be crystallized in the structural type F_{m3m} of cubic fluorite with the incorporation of praseodymium and zirconium cations into the lattice. The addition of Pr to mixed ceria–zirconia led to increased reducibility during TPR-H₂ experiments and stronger parameter changes during in situ XRD in hydrogen, which together confirm the higher reactivity of lattice oxygen. The introduction of nickel into the catalyst composition directly at the stage of support synthesis (one-pot) allowed a significant amount of nickel to be incorporated into the fluorite structure, leading to both an increase in the defectiveness of the oxide and the formation of highly dispersed particles of metallic nickel, strongly bound to the support oxide during reduction pretreatment. The introduction of Pr into the oxide support significantly increased the activity of catalysts in syngas production, which is most likely associated with facilitating the oxidant molecule activation, thus promoting the redox mechanism of MDR. The use of Pr-doped ceria–zirconia as a support made it possible to achieve excellent stability due to the high dispersion of metal particles, the optimal strength of the metal–support interaction, and lattice oxygen activity in reactions of oxidant activation and the gasification of carbon precursors. The 5%Ni/Ce_{0.75}Zr_{0.15}Pr_{0.1}O₂ catalyst showed stable performance in the MDR reaction for 30 h at a CH₄ conversion ~40% and a H₂ yield ~20% ($T = 700$ °C; $\tau = 10$ ms).

Author Contributions: Methodology, M.A., E.S., Y.B. and M.S.; investigation, K.V., V.F., A.H. and O.B.; writing—original draft preparation, M.A.; writing—review and editing, E.S., Y.B. and M.S.; supervision, V.S.; project administration, M.S.; funding acquisition, M.S. All authors have read and agreed to the published version of the manuscript.

Funding: This research was funded by the Russian Science Foundation (grant number 18-73-10167).

Data Availability Statement: Not applicable.

Acknowledgments: The authors acknowledge the Shared Research Center “VTAN” of the Novosibirsk State University, supported by the Ministry of Science and Higher Education of the Russian Federation via agreement #075-12-2021-697, for their help in the HRTEM investigation. The authors would also like to personally thank A.V. Ishchenko for carrying out HRTEM studies and A.A. Leonova for conducting experiments of nitrogen adsorption–desorption.

Conflicts of Interest: The authors declare no conflict of interest.

References

- Jang, W.-J.; Shim, J.-O.; Kim, H.-M.; Yoo, S.-Y.; Roh, H.-S. A review on dry reforming of methane in aspect of catalytic properties. *Catal. Today* **2019**, *324*, 15–26. [[CrossRef](#)]
- Aresta, M.; Dibenedetto, A. Utilisation of CO₂ as a chemical feedstock: Opportunities and challenges. *Dalton Trans.* **2007**, *28*, 2975–2992. [[CrossRef](#)] [[PubMed](#)]
- Verykios, X.E. Catalytic dry reforming of natural gas for the production of chemicals and hydrogen. *Int. J. Hydrog Energy* **2003**, *28*, 1045–1063. [[CrossRef](#)]

4. Su, B.; Wang, Y.; Xu, Z.; Han, W.; Jin, H.; Wang, H. Novel ways for hydrogen production based on methane steam and dry reforming integrated with carbon capture. *Energy Convers. Manag.* **2022**, *270*, 116199. [[CrossRef](#)]
5. Alipour, Z.; Borugadda, V.B.; Wang, H.; Dalai, A.K. Syngas production through dry reforming: A review on catalysts and their materials, preparation methods and reactor type. *Chem. Eng. J.* **2023**, *452 Pt 3*, 139416. [[CrossRef](#)]
6. Abdulrasheed, A.; Jalil, A.A.; Gambo, Y.; Ibrahima, M.; Hambali, H.U.; Hamid, M.Y.S. A review on catalyst development for dry reforming of methane to syngas: Recent advances. *Renew. Sustain. Energy Rev.* **2019**, *108*, 175–193. [[CrossRef](#)]
7. Yentekakis, I.V.; Panagiotopoulou, P.; Artemakis, G. A review of recent efforts to promote dry reforming of methane (DRM) to syngas production via bimetallic catalyst formulation. *Appl. Catal. B Environ.* **2021**, *296*, 120210. [[CrossRef](#)]
8. Akri, M.; Zhao, S.; Li, X.; Zang, K.; Lee, A.F.; Isaacs, M.A.; Xi, W.; Gangarajula, Y.; Luo, J.; Ren, Y.; et al. Atomically dispersed nickel as coke-resistant active sites for methane dry reforming. *Nat. Commun.* **2019**, *10*, 5181. [[CrossRef](#)]
9. Zhang, X.; Deng, J.; Lan, T.; Shen, T.; Zhong, Q.; Ren, W.; Zhang, D. Promoting Methane Dry Reforming over Ni Catalysts via Modulating Surface Electronic Structures of BN Supports by Doping Carbon. *ACS Catal.* **2022**, *12*, 14152–14161. [[CrossRef](#)]
10. Rosli, S.N.A.; Abidin, S.Z.; Osazuwa, O.U.; Fan, X.; Jiao, Y. The effect of oxygen mobility/vacancy on carbon gasification in nano catalytic dry reforming of methane: A review. *J. CO₂ Util.* **2022**, *63*, 102109. [[CrossRef](#)]
11. Chaudhary, M.L.; Al-Fatesh, A.S.; Kumar, R.; Lanre, M.S.; Frusteri, F.; AlReshaidan, S.B.; Ibrahim, A.A.; Abasaheed, A.E.; Fakeeha, A.H. Promotional effect of addition of ceria over yttria-zirconia supported Ni based catalyst system for hydrogen production through dry reforming of methane. *Int. J. Hydrog Energy* **2022**, *47*, 20838–20850. [[CrossRef](#)]
12. Zhao, K.; Zhang, R.; Gao, Y.; Lin, Y.; Liu, A.; Wang, X.; Zheng, A.; Huang, Z.; Zhao, Z. High syngas selectivity and near pure hydrogen production in perovskite oxygen carriers for chemical looping steam methane reforming. *Fuel Process. Technol.* **2022**, *236*, 107398. [[CrossRef](#)]
13. Li, R.-J.; Zhang, J.-P.; Shi, J.; Li, K.-Z.; Liu, H.-L.; Zhu, X. Regulation of metal-support interface of Ni/CeO₂ catalyst and the performance of low temperature chemical looping dry reforming of methane. *J. Fuel Chem. Technol.* **2022**, *50*, 1458–1470. [[CrossRef](#)]
14. Vijay, S.; Ju, W.; Brückner, S.; Tsang, S.C.; Strasser, P.; Chan, K. Unified mechanistic understanding of CO₂ reduction to CO on transition metal and single atom catalysts. *Nat. Catal.* **2021**, *4*, 1024–1031. [[CrossRef](#)]
15. Yu, K.; Lou, L.; Liu, S.; Zhou, W. Asymmetric Oxygen Vacancies: The Intrinsic Redox Active Sites in Metal Oxide Catalyst. *Adv. Sci.* **2020**, *7*, 1901970. [[CrossRef](#)]
16. Yang, J.; Hu, S.; Fang, Y.; Hoang, S.; Li, L.; Yang, W.; Liang, Z.; Wu, J.; Hu, J.; Xiao, W.; et al. Oxygen Vacancy Promoted O₂ Activation over Perovskite Oxide for Low-Temperature CO Oxidation. *ACS Catal.* **2019**, *9*, 9751–9763. [[CrossRef](#)]
17. Wu, L.; Xie, X.; Ren, H.; Gao, X. A short review on nickel-based catalysts in dry reforming of methane: Influences of oxygen defects on anti-coking property. *Mater. Today Proc.* **2021**, *42*, 153–160. [[CrossRef](#)]
18. Salcedo, A.; Lustemberg, P.G.; Rui, N.; Palomino, R.M.; Liu, Z.; Nemsak, S.; Senanayake, S.D.; Rodriguez, J.A.; Ganduglia-Pirovano, M.V.; Irigoyen, B. Reaction Pathway for Coke-Free Methane Steam Reforming on a Ni/CeO₂ Catalyst: Active Sites and the Role of Metal–Support Interactions. *ACS Catal.* **2021**, *11*, 8327–8337. [[CrossRef](#)]
19. McFarland, E.W.; Metiu, H. Catalysis by Doped Oxides. *Chem. Rev.* **2013**, *113*, 4391–4427. [[CrossRef](#)]
20. Shi, J.; Li, H.; Genest, A.; Zhao, W.; Qi, P.; Wang, T.; Rupprechter, G. High-performance water gas shift induced by asymmetric oxygen vacancies: Gold clusters supported by ceria-praseodymia mixed oxides. *Appl. Catal. B Environ.* **2022**, *301*, 120789. [[CrossRef](#)]
21. Vasiliades, M.A.; Djinović, P.; Davlyatova, L.F.; Pintar, A.; Efstathiou, A.M. Origin and reactivity of active and inactive carbon formed during DRM over Ni/Ce_{0.38}Zr_{0.62}O_{2-δ} studied by transient isotopic techniques. *Catal. Today* **2018**, *299*, 201–211. [[CrossRef](#)]
22. Puigdollers, A.R.; Schlexer, P.; Tosoni, S.; Pacchioni, G. Increasing Oxide Reducibility: The Role of Metal/Oxide Interfaces in the Formation of Oxygen Vacancies. *ACS Catal.* **2017**, *7*, 6493–6513. [[CrossRef](#)]
23. Teh, L.P.; Setiabudi, H.D.; Timmiati, S.N.; Aziz, M.A.A.; Annuar, N.H.R.; Ruslan, N.N. Recent progress in ceria-based catalysts for the dry reforming of methane: A review. *Chem. Eng. Sci.* **2021**, *239*, 116606. [[CrossRef](#)]
24. Salaev, M.A.; Liotta, L.F.; Vodyankina, O.V. Lanthanoid-containing Ni-based catalysts for dry reforming of methane: A review. *Int. J. Hydrog. Energy* **2022**, *47*, 4489–4535. [[CrossRef](#)]
25. Makri, M.M.; Vasiliades, M.A.; Petalidou, K.C.; Efstathiou, A.M. Effect of support composition on the origin and reactivity of carbon formed during dry reforming of methane over 5wt%Ni/Ce_{1-x}M_xO₂ (M = Zr⁴⁺, Pr³⁺) catalysts. *Catal. Today* **2016**, *259*, 150–164. [[CrossRef](#)]
26. Lanre, M.S.; Abasaheed, A.E.; Fakeeha, A.H.; Ibrahim, A.A.; Al-Awadi, A.S.; bin Jumah, A.; Al-Mubaddel, F.S.; Al-Fatesh, A.S. Lanthanum–Cerium-Modified Nickel Catalysts for Dry Reforming of Methane. *Catalysts* **2022**, *12*, 715. [[CrossRef](#)]
27. Zhang, F.; Liu, Z.; Zhang, S.; Akter, N.; Palomino, R.M.; Vovchok, D.; Orozco, I.; Salazar, D.; Rodriguez, J.A.; Llorca, J.; et al. In situ elucidation of the active state of Co–CeO_x catalysts in the dry reforming of methane: The important role of the reducible oxide support and interactions with cobalt. *ACS Catal.* **2018**, *8*, 3550–3560. [[CrossRef](#)]
28. Lu, M.; Zhang, X.; Deng, J.; Kuboon, S.; Faungnawakij, K.; Xiao, S.; Zhang, D. Coking resistant dry reforming of methane over BN–nanoceria interface-confined Ni catalysts. *Catal. Sci. Technol.* **2020**, *10*, 4237–4244. [[CrossRef](#)]
29. Boaro, M.; Colussi, S.; Trovarelli, A. Ceria-Based Materials in Hydrogenation and Reforming Reactions for CO₂ Valorization. *Front. Chem.* **2019**, *7*, 28. [[CrossRef](#)]
30. Liu, B.; Li, W.; Song, W.; Liu, J. Carbonate-mediated Mars–van Krevelen mechanism for CO oxidation on cobalt-doped ceria catalysts: Facet-dependence and coordination-dependence. *Phys. Chem. Chem. Phys.* **2018**, *20*, 16045–16059. [[CrossRef](#)]

31. Sadykov, V.A.; Simonov, M.N.; Mezentseva, N.V.; Pavlova, S.N.; Fedorova, Y.E.; Bobin, A.S.; Bepalko, Y.N.; Ishchenko, A.V.; Krieger, T.A.; Glazneva, T.S.; et al. Ni-loaded nanocrystalline ceria-zirconia solid solutions prepared via modified Pechini route as stable to coking catalysts of CH₄ dry reforming. *Open Chem.* **2016**, *14*, 363–376. [[CrossRef](#)]
32. Smirnova, M.Y.; Pavlova, S.N.; Krieger, T.A.; Bepalko, Y.N.; Anikeev, V.I.; Chesalov, Y.A.; Kaichev, V.V.; Mezentseva, N.V.; Sadykov, V.A. The synthesis of Ce_{1-x}Zr_xO₂ oxides in supercritical alcohols and catalysts for carbon dioxide reforming of methane on their basis. *Russ. J. Phys. Chem. B* **2017**, *12*, 15–28. [[CrossRef](#)]
33. Vasiliades, M.A.; Makri, M.M.; Djinić, P.; Erjavec, B.; Pintar, A.; Efstathiou, A.M. Dry reforming of methane over 5 wt% Ni/Ce_{1-x}Pr_xO₂-catalysts: Performance and characterisation of active and inactive carbon by transient isotopic techniques. *Appl. Catal. B Environ.* **2016**, *197*, 168–183. [[CrossRef](#)]
34. Sinev, M.Y.; Graham, G.W.; Haack, L.P.; Shelef, M. Kinetic and structural studies of oxygen availability of the mixed oxides Pr_{1-x}M_xO_y (M = Ce, Zr). *J. Mater. Res.* **1996**, *11*, 1960–1971. [[CrossRef](#)]
35. Niu, G.; Zoellner, M.H.; Schroeder, T.; Schaefer, A.; Jhang, J.H.; Zielasek, V.; Bäumer, M.; Wilkens, H.; Wollschlager, J.; Olbrich, R.; et al. Controlling the physics and chemistry of binary and ternary praseodymium and cerium oxide systems. *Phys. Chem. Chem. Phys.* **2015**, *17*, 24513–24540. [[CrossRef](#)]
36. Kambolis, A.; Matralis, H.; Trovarelli, A. Papadopoulou, Ch. Ni/CeO₂-ZrO₂ catalysts for the dry reforming of methane. *Appl. Catal. A* **2010**, *377*, 16–26. [[CrossRef](#)]
37. Hirano, M.; Hirai, K. Effect of hydrolysis conditions on the direct formation of nanoparticles of ceria-zirconia solid solutions from acidic aqueous solutions. *J. Nanopart. Res.* **2003**, *5*, 147–156. [[CrossRef](#)]
38. Pradeep, E.; Habu, T.; Tooriyama, H.; Ohtani, M.; Kobihiro, K. Ultra-simple synthetic approach to the fabrication of CeO₂-ZrO₂ mixed nanoparticles into homogeneous, domain, and core-shell structures in mesoporous spherical morphologies using supercritical alcohols. *J. Supercrit. Fluids* **2015**, *97*, 217–223. [[CrossRef](#)]
39. Montoya, J.A.; Romero-Pascual, E.; Gimón, C.; Del Angel, P.; Monzón, A. Methane reforming with CO₂ over Ni/ZrO₂-CeO₂ catalysts prepared by sol-gel. *Catal. Today* **2000**, *63*, 71–85. [[CrossRef](#)]
40. Luisetto, I.; Tuti, S.; Romano, C.; Boaro, M.; Di Bartolomeo, E.; Kesavan, J.K.; Kumar, S.S.; Selvakumar, K. Dry reforming of methane over Ni supported on doped CeO₂: New insight on the role of dopants for CO₂ activation. *J. CO₂ Util.* **2019**, *30*, 63–78. [[CrossRef](#)]
41. Kuznetsova, T.G.; Sadykov, V.A.; Moroz, E.M.; Trukhan, S.N.; Paukshtis, E.A.; Kolomiichuk, V.N.; Burgina, E.B.; Zaikovskii, V.I.; Fedotov, M.A.; Lunin, V.V.; et al. Preparation of Ce-Zr-O composites by a polymerized complex method. *Stud. Surf. Sci. Catal.* **2002**, *143*, 659–667. [[CrossRef](#)]
42. Basile, F.; Mafessanti, R.; Fasolini, A.; Fornasari, G.; Lombardi, E.; Vaccari, A. Effect of synthetic method on CeZr support and catalytic activity of related Rh catalyst in the oxidative reforming reaction. *J. Eur. Ceram.* **2019**, *39*, 41–52. [[CrossRef](#)]
43. Cai, W.; Dong, J.; Chen, Q.; Xu, T.; Zhai, S.; Liu, X.; Cui, L.; Zhang, S. One-pot microwave-assisted synthesis of Cu-Ce_{0.8}Zr_{0.2}O₂ with flower-like morphology: Enhanced stability for ethanol dry reforming. *Adv. Powder Technol.* **2020**, *31*, 3874–3881. [[CrossRef](#)]
44. Manjunatha, S.; Dharmaprasanth, M.S. Thermal stability, optical and Photoluminescence properties of spherical Ce_xZr_{1-x}O₂ (x = 0.05) crystalline blue-emitting nanophosphors synthesized by microwave method. *Mater. Res. Express* **2018**, *5*, 035043. [[CrossRef](#)]
45. Guo, J.; Xin, X.; Zhang, X.; Zhang, S. Ultrasonic-induced synthesis of high surface area colloids CeO₂-ZrO₂. *J. Nanopart. Res.* **2009**, *11*, 737–741. [[CrossRef](#)]
46. Khani, Y.; Bahadoran, F.; Shariatnia, Z.; Varmazyari, M.; Safari, N. Synthesis of highly efficient and stable Ni/Ce_xZr_{1-x}Gd_xO₄ and Ni/X-Al₂O₃ (X = Ce, Zr, Gd, Ce-Zr-Gd) nanocatalysts applied in methane reforming reactions. *Ceram. Int.* **2020**, *46*, 25122–25135. [[CrossRef](#)]
47. Guo, T.; Du, J.; Wu, J.; Li, J. Enhanced properties of solid solution (CeZr)O₂ modified with metal oxides for catalytic oxidation of low-concentration methane. *Chin. J. Chem. Eng.* **2017**, *25*, 187–192. [[CrossRef](#)]
48. Lovell, E.; Horlyck, J.; Scott, J.; Amal, R. Flame spray pyrolysis-designed silica/ceria-zirconia supports for the carbon dioxide reforming of methane. *Appl. Catal.* **2017**, *546*, 47–57. [[CrossRef](#)]
49. Veriansyah, B.; Park, H.; Kim, J.D.; Min, B.K.; Shin, Y.H.; Lee, Y.W.; Kim, J. Characterization of surface-modified ceria oxide nanoparticles synthesized continuously in supercritical methanol. *J. Supercrit. Fluids* **2009**, *50*, 283–291. [[CrossRef](#)]
50. Hakuta, Y.; Hayashi, H.; Arai, K. Fine particle formation using supercritical fluids. *Curr. Opin. Solid State Mater. Sci.* **2003**, *7*, 341–351. [[CrossRef](#)]
51. Cabanas, A.; Darr, J.A.; Lester, E.; Poliakov, M. A continuous and clean one-step synthesis of nano-particulate Ce_{12x}Zr_xO₂ solid solutions in near-critical water. *Chem. Commun.* **2000**, *11*, 901–902. [[CrossRef](#)]
52. Darr, J.A.; Poliakov, M. New Directions in Inorganic and Metal-Organic Coordination Chemistry in Supercritical Fluids. *Chem. Rev.* **1999**, *99*, 495–541. [[CrossRef](#)]
53. Simonov, M.; Bepalko, Y.; Smal, E.; Valeev, K.; Fedorova, V.; Krieger, T.; Sadykov, V. Nickel-containing ceria-zirconia doped with Ti and Nb. Effect of support composition and preparation method on catalytic activity in methane dry reforming. *Nanomaterials* **2020**, *10*, 1281. [[CrossRef](#)]
54. Lustemberg, P.G.; Mao, Z.; Salcedo, A.; Irigoyen, B.; Ganduglia-Pirovano, M.V.; Campbell, C.T. Nature of the active sites on Ni/CeO₂ catalysts for methane conversions. *ACS Catal.* **2021**, *11*, 10604–10613. [[CrossRef](#)] [[PubMed](#)]
55. Li, M.; van Veen, A.C. Tuning the catalytic performance of Ni-catalysed dry reforming of methane and carbon deposition via Ni-CeO_{2-x} interaction. *Appl. Catal. B Environ.* **2018**, *237*, 641–648. [[CrossRef](#)]

56. Anchieta, C.G.; Assaf, E.M.; Assaf, J.M. Syngas production by methane tri-reforming: Effect of Ni/CeO₂ synthesis method on oxygen vacancies and coke formation. *J. CO₂ Util.* **2022**, *56*, 101853. [[CrossRef](#)]
57. Lyu, Y.; Jocz, J.N.; Xu, R.; Stavitski, E.; Sievers, C. Nickel speciation and methane dry reforming performance of Ni/Ce_xZr_{1-x}O₂ prepared by different synthesis methods. *ACS Catal.* **2020**, *10*, 11235–11252. [[CrossRef](#)]
58. Bepalko, Y.; Smal, E.; Simonov, M.; Valeev, K.; Fedorova, V.; Krieger, T.; Cherepanova, S.; Ishchenko, A.; Rogov, V.; Sadykov, V. Novel Ni/Ce(Ti)ZrO₂ catalysts for methane dry reforming prepared in supercritical alcohol media. *Energies* **2020**, *13*, 3365. [[CrossRef](#)]
59. Rietveld, H.M. A profile refinement method for nuclear and magnetic structures. *J. Appl. Crystallogr.* **1969**, *2*, 65–71. [[CrossRef](#)]
60. Leofanti, G.; Padovan, M.; Tozzola, G.; Venturelli, B. Surface area and pore texture of catalysts. *Catal. Today* **1998**, *41*, 207–219. [[CrossRef](#)]
61. Gregg, S.J.; Sing, K.S.W. *Adsorption, Surface Area and Porosity*; Academic Press: London, UK, 1982.
62. Ballauri, S.; Sartoretti, E.; Novara, C.; Giorgis, F.; Piumetti, M.; Fino, D.; Russo, N.; Bensaid, S. Wide range temperature stability of palladium on ceria-praseodymia catalysts for complete methane oxidation. *Catal. Today* **2022**, *390–391*, 185–197. [[CrossRef](#)]
63. Rajendran, M.; Mallick, K.K.; Bhattacharya, A.K. Combustion synthesis, powder characteristics and crystal structure of phases in Ce–Pr–O system. *J. Mater. Sci.* **1998**, *33*, 5001–5006. [[CrossRef](#)]
64. Li, Z.; Li, L.; Yuan, Q.; Feng, W.; Xu, J.; Sun, L.; Song, W.; Yan, C. Sustainable and Facile Route to Nearly Monodisperse Spherical Aggregates of CeO₂ Nanocrystals with Ionic Liquids and Their Catalytic Activities for CO Oxidation. *J. Phys. Chem. C* **2008**, *112*, 18405–18411. [[CrossRef](#)]
65. Takeguchi, T.; Furukawa, S.N.; Inoue, M. Hydrogen spillover from NiO to the large surface area CeO₂-ZrO₂ solid solutions and activity of the NiO/CeO₂-ZrO₂ catalysts for partial oxidation of methane. *J. Catal.* **2001**, *202*, 14–24. [[CrossRef](#)]
66. Iglesias, I.; Baronetti, G.; Marino, F. Ni/Ce_{0.95}M_{0.05}O_{2-d} (M = Zr, Pr, La) for methane steam reforming at mild conditions. *Int. J. Hydrog. Energy* **2017**, *42*, 29735–29744. [[CrossRef](#)]
67. Jalowiecki-Duhamel, L.; Zarrou, H.; D’Huysser, A. Hydrogen production at low temperature from methane on cerium and nickel based mixed oxides. *Int. J. Hydrog. Energy* **2008**, *33*, 5527–5534. [[CrossRef](#)]
68. Smal, E.; Bepalko, Y.; Arapova, M.; Fedorova, V.; Valeev, K.; Ereemeev, N.; Sadvovskaya, E.; Krieger, T.; Glazneva, T.; Sadykov, V.; et al. Carbon formation during methane dry reforming over Ni-containing ceria-zirconia catalysts. *Nanomaterials* **2022**, *12*, 3676. [[CrossRef](#)]
69. Fakeeha, A.H.; Kurdi, A.; Al-Baqmaa, Y.A.; Ibrahim, A.A.; Abasaeed, A.E.; Al-Fatesh, A.S. Performance Study of Methane Dry Reforming on Ni/ZrO₂ Catalyst. *Energies* **2022**, *15*, 3841. [[CrossRef](#)]
70. Shine, S.; Su, N.Y.; Hoon, H.G.; In, P.J.; Tae, S.H.; Kwan-Young, L.; Ju, M.D. Dry reforming of methane over Ni/ZrO₂-Al₂O₃ catalysts: Effect of preparation methods. *J. Taiwan Inst. Chem. Eng.* **2018**, *90*, 25–32. [[CrossRef](#)]
71. Ibrahim, A.A.; Fakeeha, A.H.; Lanre, M.S.; Al-Awadi, A.S.; Alreshaidan, S.B.; Albaqmaa, Y.A.; Adil, S.F.; Al-Zahrani, A.A.; Abasaeed, A.E.; Al-Fatesh, A.S. The Effect of Calcination Temperature on Various Sources of ZrO₂ Supported Ni Catalyst for Dry Reforming of Methane. *Catalysts* **2022**, *12*, 361. [[CrossRef](#)]
72. Al-Fatesh, A.S.; Arafat, Y.; Ibrahim, A.A.; Kasim, S.O.; Alharthi, A.; Fakeeha, A.H.; Abasaeed, A.E.; Bonura, G.; Frusteri, F. Catalytic Behaviour of Ce-Doped Ni Systems Supported on Stabilized Zirconia under Dry Reforming Conditions. *Catalysts* **2019**, *9*, 473. [[CrossRef](#)]

Disclaimer/Publisher’s Note: The statements, opinions and data contained in all publications are solely those of the individual author(s) and contributor(s) and not of MDPI and/or the editor(s). MDPI and/or the editor(s) disclaim responsibility for any injury to people or property resulting from any ideas, methods, instructions or products referred to in the content.